APL Materials

Structural characterization of the $LaInO_3$/$BaSnO_3$ interface via synchrotron scattering

Cite as: APL Mater. **7**, 031108 (2019); https://doi.org/10.1063/1.5084058
Submitted: 03 December 2018 . Accepted: 03 February 2019 . Published Online: 15 March 2019

Claudia Lau, Youjung Kim, Stephen Albright, Kookrin Char, C. H. Ahn, and F. J. Walker

Structural characterization of the $LaInO_3/BaSnO_3$ interface via synchrotron scattering

Cite as: APL Mater. 7, 031108 (2019); doi: 10.1063/1.5084058
Submitted: 3 December 2018 • Accepted: 3 February 2019 •
Published Online: 15 March 2019 • Corrected: 13 June 2019

Claudia Lau,[1] Youjung Kim,[2] Stephen Albright,[1] Kookrin Char,[2] C. H. Ahn,[1,3] and F. J. Walker[3]

AFFILIATIONS

[1]Department of Physics, Yale University, New Haven, Connecticut 06520, USA
[2]Department of Physics and Astronomy, Institute of Applied Physics, Seoul National University, Seoul 08826, South Korea
[3]Department of Applied Physics, Yale University, New Haven, Connecticut 06520, USA

ABSTRACT

The alkaline earth stannate $BaSnO_3$ is a semiconductor with high carrier mobility at room-temperature when doped with La^{3+}. When a thin epitaxial layer of $LaInO_3$ is grown on lightly doped $BaSnO_3$, a polar discontinuity between the orthorhombic, polar $LaInO_3$ and the cubic, nonpolar $Ba_{0.998}La_{0.002}SnO_3$ leads to an electronic reconstruction, where $LaInO_3$ remotely dopes $Ba_{0.998}La_{0.002}SnO_3$, creating carriers for high mobility devices. We determine aspects of the crystalline structure of the $LaInO_3/BaSnO_3$ film that affect the polar discontinuity using synchrotron x-ray diffraction. Specifically, we examine the role of oxygen octahedral rotations and anti-parallel cation displacements in influencing the polarization of the $LaInO_3/BaSnO_3$ interface. These structural distortions are characterized by measuring half-order Bragg peaks of thin film $LaInO_3/BaSnO_3/SrTiO_3$ heterostructures grown by pulsed laser deposition. We find that for films as thin as 3 unit cells, epitaxial $LaInO_3$ has 2 distinct domains, one with the same Glazer tilt pattern as that of bulk $LaInO_3$, $a^+b^-b^-$, and a second rotated 90° in-plane from the first and having tilt pattern $b^-a^+b^-$. Additionally, we observe a sudden and large increase in cation displacements along the [011] and [101] directions across the $LaInO_3/BaSnO_3$ interface due to the strength of the octahedral rotations.

The alkaline earth stannates are perovskite oxides with chemical formula $ASnO_3$, where A denotes an alkaline earth metal.[1] When electron doped, they display high carrier mobility at room temperature,[2,3] which can be leveraged in all-epitaxial oxide heterostructures as the foundation of novel multifunctional devices. Of particular interest is barium stannate, $BaSnO_3$, which, in addition to its high mobility, is a transparent conducting oxide (or TCO) and possesses excellent thermal stability, maintaining highly stable oxygen stoichiometry and conduction behavior against annealing in various atmospheres at temperatures up to 1000 °C.[2,3] These properties make $BaSnO_3$ useful for devices such as high-temperature sensors[4] and solar cells.[5]

Bulk single crystal lanthanum-doped barium stannate $Ba_{0.93}La_{0.07}SnO_3$ (or LBSO) has a mobility of 100 to 320 $cm^2/(Vs)$,[2,3,6] a factor of 10 better than the mobility of strontium titanate ($SrTiO_3$ or STO), which is the current standard for perovskite oxide-based devices. Thin film BSO[7,8] has been demonstrated to have a mobility as high as 150 $cm^2/(Vs)$ on $PrScO_3$ (110)[9] and 183 $cm^2/(Vs)$ on $DyScO_3$ (001).[10] LBSO on STO (001)[11] has a measured mobility of 70–120 $cm^2/(Vs)$.[2,12–14]

Researchers have demonstrated an all-oxide field effect transistor (or FET) using $BaSnO_3$ as the conducting channel[15] and either aluminum oxide (Al_2O_3),[16] hafnium oxide (HfO_2),[17,18] or lanthanum indate ($LaInO_3$)[19–21] as the gate dielectric. We investigate the all-perovskite $LaInO_3/BaSnO_3/SrTiO_3$ FET, which has a large on/off ratio, $I_{on}/I_{off} = 10^7$, and high field effect mobility, $\mu \sim 90$ $cm^2/(Vs)$.[19] This high mobility may be due to the polar $LaInO_3$ gate dielectric remotely doping[22] the $BaSnO_3$ conducting channel, resulting in an electronic reconstruction at the interface. Interfacial electronic reconstruction and its creation of high mobility carriers has

been observed and studied in similar polar/nonpolar structures, such as $LaAlO_3/SrTiO_3$[23,24] and $RTiO_3/SrTiO_3$[25–27] materials.[28]

Nonpolar $BaSnO_3$ (or BSO) is cubic in structure, with lattice parameter a = 4.116 Å, and is well lattice-matched to polar $LaInO_3$ (or LIO), which has lattice parameters a = 4.124 Å and $b = c$ = 4.108 Å.[29] LIO possesses strong octahedral rotations, displacement of the oxygen anions from their face-centered positions, and displacement of the La^{3+} cations from their corner positions in large anti-parallel shifts. Owing to these distortions, the crystalline structure of LIO is best described by an orthorhombic unit cell consisting of 2 La^{3+} cations, 2 In^{3+} cations, and 6 O^{2-} anions with lattice parameters a = 5.940 Å, b = 8.216 Å, and c = 5.723 Å.[29]

In Glazer notation, the LIO octahedral tilt pattern is $a^+b^-b^-$ (i.e., space group *Pnma*), where a^+ denotes in-phase rotation by angle α around the x-axis and b^-b^- denotes anti-phase rotation by angle $\beta = \gamma$ around the y and z axes.[30] For in-phase rotation [see Fig. 1(a)], octahedra in adjacent perovskite layers along the rotational axis rotate in the same direction, while for anti-phase rotation [see Figs. 1(b) and 1(c)], octahedra in adjacent perovskite layers along the rotational axis rotate in opposing directions. Octahedral rotation around each of the 3 axes creates a unique set of half-order Bragg peaks:

in-phase rotation along the x-axis creates peaks at ½(*eoo*) for $k \neq l$,
anti-phase rotation along the y-axis creates peaks at ½(*ooo*) for $h \neq l$,
and anti-phase rotation along the z-axis creates peaks at ½(*ooo*) for $h \neq k$,

where *o* denotes an odd number and *e* denotes an even number. In response to these octahedral rotations, the La^{3+} cations are displaced along the [011] direction by vectors of magnitude d_1 and d_2, [see Fig. 1(d)], resulting in strong reflections at ½(*oee*). These cation shifts also contribute to ½(*ooo*) reflections due to anti-phase oxygen octahedral rotation, as discussed above.

Epitaxial thin films of $LaInO_3/BaSnO_3$ are grown on $SrTiO_3$ (001) substrates by pulsed laser deposition (or PLD). LIO film thicknesses range from 1.2 to 10.0 nm [i.e., 3–24 unit cells (uc)], and the BSO thickness is held constant at 120 nm (~290 uc).

The crystalline structure of the $LaInO_3/BaSnO_3$ thin films is investigated using synchrotron x-ray diffraction. Data are collected on the X-ray Science Division beamline 33-ID at the Advanced Photon Source, Argonne National Laboratory. Diffraction measurements are taken at room temperature using an x-ray energy of 12.6 keV (λ = 0.984 Å). During measurement, the samples are mounted inside a dome of flowing helium gas to minimize background scattering. The diffracted intensity is measured using a solid state area detector at 300 K for each sample. Measurements are taken at half-order Bragg peaks (i.e., at half-integer values of h,k,l) of the $BaSnO_3$ film. At a thickness of 120 nm, the $BaSnO_3$ film is relaxed relative to the $SrTiO_3$ substrate and cubic with lattice parameter a = 4.11 Å, allowing us to isolate the $BaSnO_3$ Bragg peaks at multiples of the $SrTiO_3$ in-plane indices $h = k$ = 3.905 Å/4.11 Å = 0.95. The LIO is tetragonally strained to the BSO, with c/a = 4.15 Å/4.11 Å = 1.01.

From the presence and absence of specific half-order peaks, we find that for films as thin as 3 uc, the LIO film has one domain with the same Glazer tilt pattern as bulk LIO,

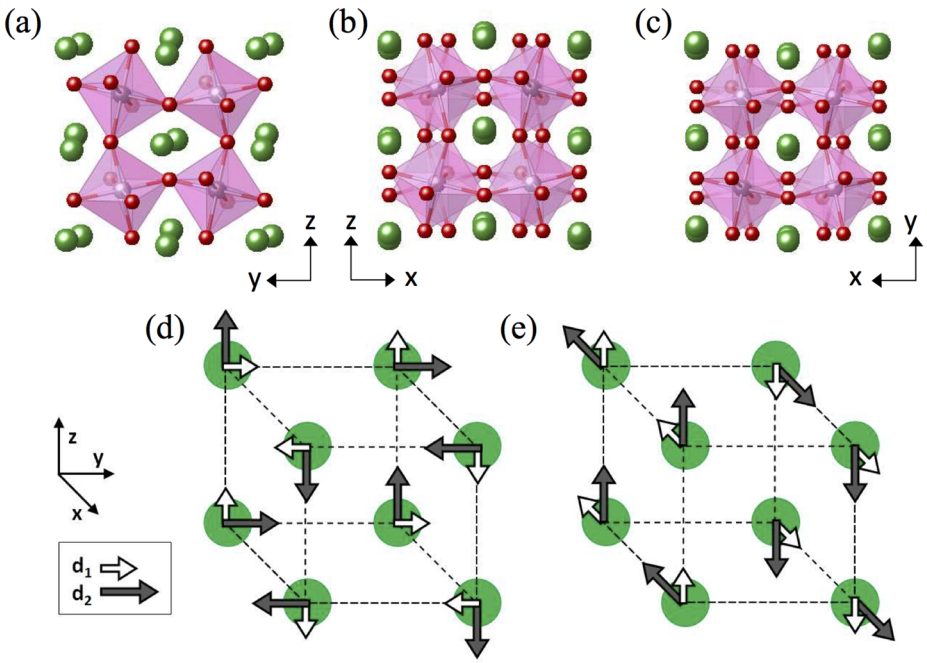

FIG. 1. LIO has Glazer tilt pattern $a^+b^-b^-$, where (a) a^+ denotes in-phase rotation of oxygen octahedra by angle α along the x-axis and (b) and (c) b^-b^- denote anti-phase rotation of oxygen octahedra by angle $\beta = \gamma$ along both the y and z axes. (d) Rotation of the oxygen octahedra force strong anti-parallel shifts of the La^{3+} cations by values d_1 and d_2 where $d_1 < d_2$. In domain 1, these displacements occur in the yz plane. (e) In domain 2, which is rotated 90° in-plane from domain 1 and has Glazer tilt pattern $b^-a^+b^-$, displacements occur in the xz plane.

(i.e., $a^+b^-b^-$) and that the film also includes a second domain rotated 90° in-plane from the first, with rotation pattern $b^-a^+b^-$. Octahedral rotations of the second domain result in peaks $\frac{1}{2}(oeo)$ for $h \neq l$ and $\frac{1}{2}(ooo)$ for $k \neq l$. Anti-parallel cation displacements along the [101] direction for this second domain, as shown in Fig. 1(e), result in peaks $\frac{1}{2}(eoe)$. Half-order peaks from a potential third domain $b^-b^-a^+$, which would create peaks $\frac{1}{2}(ooe)$ for $h \neq k$ and $\frac{1}{2}(eeo)$, are not observed.

A comparison of the diffraction from 5 films with LIO thickness ranging from 1.2 to 10.0 nm shows that, beginning at 3.6 nm thickness, the LIO film begins to relax relative to the BSO. As shown in Fig. 2(a), while peaks $\frac{1}{2}(302)$ and $\frac{1}{2}(315)$ increase in intensity and decrease in width, as expected for the increasing film thickness, peak $\frac{1}{2}(218)$ achieves its maximum intensity for thickness 3.6 nm. The intensity of peak $\frac{1}{2}(218)$ is decreased above this thickness as the intensity is then divided between two peaks as the film relaxes to two orthorhombic domains. Because in-plane lattice parameters $a \neq b$, in the LIO 2 × 2 unit cell, the scattering from domains which would appear at the same location under the standard fourfold geometric symmetry is distinctly separated in reciprocal space once the film relaxes. As shown in the reciprocal space maps in Fig. 2(b), these two $\frac{1}{2}(218)$ peaks become distinct by thickness 10.0 nm.

We fit the diffraction to the function

$$I = A\left(\frac{\sin n2\pi(x - L)}{n2\pi(x - L)}\right)^2, \quad (1)$$

where n is the number of non-primitive LIO unit cells, and calculate a scaled integrated intensity I_{data} ~ height × width = A/n, where FWHM = $0.4428/n$. From the good agreement of the mean peak width n with the actual LIO thickness, we determine that the octahedral rotation and cation shifts occur throughout the film. Because of relaxation, for films of LIO thickness greater than 3.6 nm, the mean peak width n is decreased with a larger error. Table I shows the integrated intensities I_{data}, sorted into groups $\frac{1}{2}(eol)$, $\frac{1}{2}(oel)$, and $\frac{1}{2}(ooo)$, for our 5 films. The mean peak width n as a function of film thickness is shown in Table II.

To determine the rotation angles α, β, and γ and the magnitude of the cation displacements d_1 and d_2, we fit the half-order Bragg peak integrated intensities to a kinematic model of x-ray diffraction with a non-primitive c(2 × 2) unit cell,[31,32] allowing rotations of oxygen octahedra as well as anti-parallel La^{3+} cation displacements in the LIO film. Because LIO and BSO have cations of similar scattering strength, our x-ray measurements are not sensitive to any possible interfacial cation intermixing. We focus our analysis instead on the system's distortion from the cubic structure.

The integrated intensities are fit to a model with incoherent scattering between four domains,[33,34]

$$I = I_0 n^2 \left(\sum_{j=1}^{4} D_j |F_{hkl}|^2\right), \quad (2)$$

where the first two domains are $a^+b^-b^-$ and $b^-a^+b^-$, discussed above, the third domain has tilt pattern $a^+b^-b^-$ and is rotated 180° in-plane from domain 1, and the fourth domain has tilt pattern $b^-a^+b^-$ and is rotated 180° in-plane from domain 2. The La^{3+} cations are displaced according to the configurations shown in Figs. 1(d) and 1(e), respectively, for the first two domains, and in those same configurations rotated by 180° for the third and fourth domains.[34] n is the number of non-primitive LIO unit cells previously calculated from our fits to the peak width. The domains possess equal occupation $D_j = 1/4$, and the structure factor for each Bragg peak is

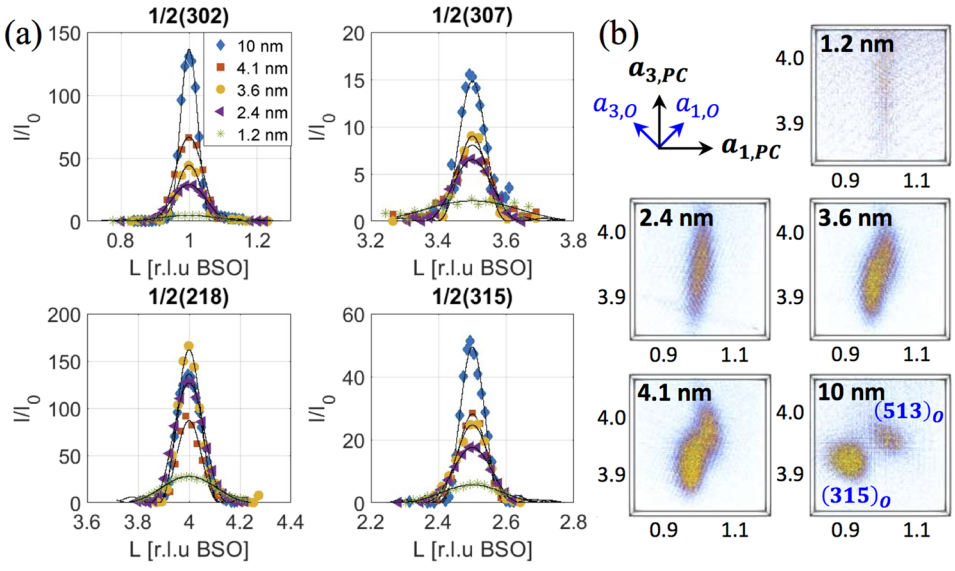

FIG. 2. (a) The pattern of half-order diffraction peaks reveals two distinct domains: $a^+b^-b^-$ and $b^-a^+b^-$. By fitting the half-order peaks to a kinematic model of x-ray diffraction, we determine the oxygen octahedral rotational angles α, β, and γ, as well as the anti-parallel displacements of the La^{3+} cations along the [011] and [101] directions. (b) From peaks further out in reciprocal space, such as $\frac{1}{2}(218)$, using the pseudocubic (PC) reciprocal lattice, we observe that the LIO film begins to relax around a thickness of 3.6 nm. Reciprocal space maps of the $\frac{1}{2}(218)$ peak clearly show peak splitting into two over thicknesses from 3.6 to 10.0 nm. In domain 1, reciprocal primitive vectors for the orthorhombic unit cell are given by $a_{1,O} = \frac{1}{2}(a_{1,PC} + a_{3,PC})$, $a_{2,O} = \frac{1}{2}a_{2,PC}$, and $a_{3,O} = \frac{1}{2}(-a_{1,PC} + a_{3,PC})$, where $a_{i,PC}$ are the reciprocal primitive vectors of the pseudocubic unit cell. For domain 2, $a_{1,O}$ and $a_{3,O}$ are switched.

TABLE I. Integrated intensities of half-order Bragg peaks ½(*eol*), ½(*oel*), and ½(*ooo*). Bolded reflections are shown in Fig. 2.

		10 nm		4.1 nm		3.6 nm		2.4 nm		1.2 nm	
	½(h k l)	I_{data}	I_{calc}	I_{data}	I_{calc}	I_{data}	I_{calc}	I_{data}	I_{calc}	I_{data}	I_{calc}
½(*eol*)	½(2 1 3)	3.9	1.6	3.3	1.4	3.3	1.2	2.7	1.3	0.8	0.5
	½(2 1 7)	9.3	7.0	5.1	7.6	7.6	6.2	8.3	6.4	3.6	3.3
	½(2 1 8)	34.6	29.5	21.4	35.7	38.7	35.4	39.5	32.2	15.0	13.0
	½(2 1 10)	30.4	19.0	9.4	24.2	22.9	24.5	26.8	23.9	12.1	10.5
	½(0 1 7)	3.5	1.9	3.0	1.8	2.3	1.3	2.3	1.4	1.0	0.8
	½(0 1 8)	20.2	36.7	52.9	43.5	51.2	43.1	42.8	38.8	16.3	14.7
	½(0 1 9)	2.3	4.1	4.4	6.2	3.3	4.6	4.2	4.8	4.4	3.8
	½(0 1 10)	9.6	20.6	25.0	27.9	23.0	27.8	21.2	27.7	10.2	12.2
	½(4 1 4)	26.9	24.1	38.3	27.4	23.6	26.5	24.3	24.7	5.6	8.0
	½(4 1 5)	1.2	2.1	1.1	2.0	1.3	1.6	1.3	1.7	7.5	9.7
½(*oel*)	**½(3 0 2)**	18.1	11.6	14.1	10.9	8.2	10.8	7.6	9.3	2.0	2.7
	½(3 0 4)	19.1	21.0	21.8	21.3	17.1	21.2	15.6	17.2	5.7	5.1
	½(3 0 5)	9.6	5.3	7.8	4.9	5.6	4.3	6.0	4.6	2.6	1.8
	½(3 0 6)	42.4	47.3	51.1	50.1	46.3	49.4	40.8	43.2	13.7	14.6
	½(3 0 7)	3.0	4.1	2.3	3.5	1.9	2.9	1.9	3.2	1.5	1.3
	½(3 0 8)	32.3	34.0	43.7	37.8	40.2	38.1	37.1	34.8	12.6	12.1
	½(3 2 2)	18.1	19.3	12.8	18.6	8.2	18.3	7.8	16.1	3.2	5.0
	½(3 2 4)	28.0	21.6	26.6	22.6	21.3	22.3	20.6	19.0	6.7	6.3
	½(3 2 7)	1.0	2.7	1.3	3.1	1.2	2.4	1.0	2.3	0.9	1.4
	½(3 2 8)	24.0	26.5	25.2	30.5	24.5	30.7	22.2	28.7	9.7	10.8
½(*ooo*)	½(3 1 3)	4.8	1.9	3.3	2.2	4.3	1.7	3.3	1.8	1.5	1.1
	½(3 1 5)	9.1	4.4	5.9	4.5	6.1	3.8	5.1	4.2	2.6	2.3
	½(3 3 3)	4.4	3.1	3.3	3.7	2.4	2.8	3.0	2.9	1.1	1.9
	½(3 3 5)	7.7	9.4	8.2	9.5	8.5	7.9	8.6	8.5	4.0	4.4

$$F_{hkl} = f_{O^{2-}} \sum_{n=1}^{24} \exp[2\pi i(hu_n + kv_n + lw_n)] + f_{La^{3+}} \sum_{n=1}^{8} \times \exp[2\pi i(hu_n + kv_n + lw_n)], \quad (3)$$

where the energy-dependent atomic scattering factor f is approximately equal to the atomic number Z, $f_{O^{2-}} \approx 8$, and $f_{La^{3+}} \approx 57$.

The integrated intensities of the half-order Bragg peaks are shown with their best fits in Table I. Because $f_{La^{3+}} > f_{O^{2-}}$, peaks ½(*hke*), which are due to cation shifts, possess higher intensity than peaks ½(*hko*), which are primarily due to octahedral rotation. Cation shifts are also the dominant scattering contribution for peaks ½(*ooo*), and therefore our data are not sufficiently sensitive to the out-of-phase rotation angles $\beta = \gamma$, which thus converge to their bulk value 12.2°. We note that these values have not been refined and expect them to be different, $\beta \neq \gamma$, owing to the inequivalent in-plane and out-of-plane pseudocubic lattice parameters $b \neq c$ induced by biaxial strain. With the relaxation of the $\beta = \gamma$ constraint, the two LIO domains are then more aptly characterized as $a^+b^-c^-$ and $b^-a^+c^-$.

We determine best fit values for in-phase rotation angle α and cation shift displacements d_1 and d_2 and find that there is no clear thickness dependence for these values. From the rotation angles α, β, and γ, we calculate the bond angle distortion $\theta_{\text{In–O–In}}$ along the x, y, and z axes, as shown in Table III.

TABLE II. Bragg peak width as a function of film thickness.

LIO thickness (nm)	No. LIO non-primitive u.c.	No. LIO non-primitive u.c. from peak fit
1.2	1.5	1.9 ± 0.5
2.4	3.0	3.5 ± 0.4
3.6	4.5	4.6 ± 0.6
4.1	5.0	4.4 ± 0.9
10.0	12	5.9 ± 1.9

TABLE III. Cation shifts, octahedral rotations, and In–O–In bond angles in LIO.

	Literature	Fit
d_1 (Å)	0.10	0.21 ± 0.03
d_2 (Å)	0.33	0.21 ± 0.03
α (deg)	13.6	12.0 ± 0.7
β (deg)	12.2	12.2
γ (deg)	12.2	12.2
$\theta_{\text{In–O–In}}$ along ⟨100⟩ (deg)	146.0	146.0
$\theta_{\text{In–O–In}}$ along ⟨010⟩ (deg)	144.0	146.3 ± 0.9
$\theta_{\text{In–O–In}}$ along ⟨001⟩ (deg)	144.0	146.3 ± 0.9

Within our model, we assume that the LIO structure is uniform across the film; reported values are therefore averages across all layers. Error bars represent the standard deviation of the refined values of all the samples.

While the larger of the two cation displacements d_2 is in good agreement with its bulk value, the smaller cation displacement d_1 is increased and the in-phase rotation angle α is decreased from the bulk. The slight decrease in angle α can be understood as a result of the LIO film being clamped to the cubic BSO and its rotation therefore being suppressed.[35] Of greater interest is the robustness of the cation displacements d_1 and d_2, which continues all the way to the LIO/BSO interface. This abrupt discontinuity in cation displacement across the interface should have interesting implications for interfacial polarization, which is critical to the system's transport properties.

In particular, we expect the out-of-plane cation displacements in the interfacial layer to play an important role in the confinement of electrons in the LIO/BSO interface. For example, in the polar catastrophe model, each LIO unit cell donates half an electron to the BSO, with net charge flowing from the polar $(LaO)^+$ to the nonpolar $(SnO_2)^0$. At a basic level, this flow is boosted by cation shift away from the interface and impeded by cation shift toward the interface. Because the cations are displaced in alternating directions over the xy plane, these two effects should cancel each other out. However, due to the large size of the cation shifts, with $d_2 = 0.08c$, the interatomic potential between the La^{3+} and O^{2-} ions across the LIO/BSO interface can be modeled by an anharmonic potential, such as the Lennard-Jones potential. In such a model, the alternating cation displacements create a nonzero, net positive potential. This potential and the corresponding interfacial polarization are intrinsic to the crystalline structure and distinct from those created by charge imbalance in the polar catastrophe model. Such interfacial polarization may be behind the 2DEG-like behavior in the LIO/BSO interface.

In summary, we have reported on the crystalline structure of epitaxial $LaInO_3/BaSnO_3$ thin films, which have been used in a high mobility field effect device, where polar $LaInO_3$ remotely dopes the stannate with electrons. Using synchrotron x-ray diffraction, we have characterized half-order Bragg peaks of $LaInO_3$ to examine the role of the large oxygen octahedral rotations found in bulk $LaInO_3$ in influencing the polarization of this system. We observe two orientational domains in the $LaInO_3$ and find that for films as thin as 3 uc, the $LaInO_3$ has bulk-like rotations and enhanced cation displacements right up to the $BaSnO_3$ interface and believe these distortions strongly influence the polarization and transport.

Work at Yale is supported by the Office of Naval Research under Grant Nos. N00014-18-1-2704 and N00014-12-1-0976. Use of the Advanced Photon Source was supported by the U. S. Department of Energy, Office of Science, Office of Basic Energy Sciences, under Contract No. DE-AC02-06CH11357. Work at SNU was supported in part by the Samsung Science and Technology Foundation under Project No. SSTF-BA1402-09.

REFERENCES

[1] S. Ismail-Beigi, F. J. Walker, S.-W. Cheong, K. M. Rabe, and C. H Ahn, APL Mater. **3**, 062510 (2015).
[2] H. J. Kim, U. Kim, H. M. Kim, T. H. Kim, H. S. Mun, B.-G. Jeon, K. T. Hong, W.-J. Lee, C. Ju, K. H. Kim, and K. Char, Appl. Phys. Express **5**, 061102 (2012).
[3] X. Luo, Y. S. Oh, A. Sirenko, P. Gao, T. A. Tyson, K. Char, and S.-W. Cheong, Appl. Phys. Lett. **100**, 172112 (2012).
[4] Y. Shimizu, Y. Fukuyama, T. Narikiyo, H. Arai, and T. Seiyama, Chem. Lett. **14**, 377 (1985).
[5] J. Park, U. Kim, and K. Char, Appl. Phys. Lett. **108**, 092106 (2016).
[6] H. J. Kim, U. Kim, T. H. Kim, J. Kim, H. M. Kim, B.-G. Jeon, W.-J. Lee, H. S. Mun, K. T Hong, J. Yu, K. Char, and K. H. Kim, Phys. Rev. B **86**, 165205 (2012).
[7] K. Ganguly, A. Prakash, B. Jalan, and C. Leighton, APL Mater. **5**, 056102 (2017).
[8] W.-J. Lee, H. J. Kim, E. Sohn, T. H. Kim, J.-Y. Park, W. Park, H. Jeong, T. Lee, J. H. Kim, K.-Y. Choi, and K. H. Kim, Appl. Phys. Lett. **108**, 082105 (2016).
[9] S. Raghavan, T. Schumann, H. Kim, J. Y. Zhang, T. A. Cain, and S. Stemmer, APL Mater. **4**, 016106 (2016).
[10] H. Paik, Z. Chen, E. Lochocki, H. A. Seidner, A. Verma, N. Tanen, J. Park, M. Uchida, S. Shang, B.-C. Zhou, M. Brützam, R. Uecker, Z.-K. Liu, D. Jena, K. M. Shen, D. A. Muller, and D. G. Schlom, APL Mater. **5**, 116107 (2017).
[11] U. K. C. Park, T. Ha, R. Kim, H. S. Mun, H. M. Kim, H. J. Kim, T. H. Kim, N. Kim, J. Yu, K. H. Kim, J. H. Kim, and K. Char, APL Mater. **2**, 056107 (2014).
[12] H. Mun, U. Kim, H. M. Kim, C. Park, T. H. Kim, H. J. Kim, K. H. Kim, and K. Char, Appl. Phys. Lett. **102**, 252105 (2013).
[13] J. Shiogai, K. Nishihara, K. Sato, and A. Tsukazaki, AIP Adv. **6**, 065305 (2016).
[14] A. Prakash, P. Xu, A. Faghaninia, S. Shukla, J. W. Ager III, C. S. Lo, and B. Jalan, Nat. Commun. **8**, 15167 (2017).
[15] K. Krishnaswamy, L. Bjaalie, B. Himmetoglu, A. Janotti, L. Gordon, and C. G. Van de Walle, Appl. Phys. Lett. **108**, 083501 (2016).
[16] C. Park, U. Kim, C. J. Ju, J. S. Park, Y. M. Kim, and K. Char, Appl. Phys. Lett. **105**, 203503 (2014).
[17] J. Shin, Y. M. Kim, Y. Kim, C. Park, and K. Char, Appl. Phys. Lett. **109**, 262102 (2016).
[18] Y. M. Kim, C. Park, U. Kim, C. Ju, and K. Char, Appl. Phys. Express **9**, 011201 (2016).
[19] U. Kim, C. Park, T. Ha, Y. M. Kim, N. Kim, C. Ju, J. Park, J. Yu, J. H. Kim, and K. Char, APL Mater. **3**, 036101 (2015).
[20] U. Kim, C. Park, Y. M. Kim, J. Shin, and K. Char, APL Mater. **4**, 071102 (2016).
[21] Y. Kim, Y. M. Kim, J. Shin, and K. Char, APL Mater. **6**, 096104 (2018).
[22] S. Chambers, T. C. Kaspar, A. Prakash, G. Haugstad, and B. Jalan, Appl. Phys. Lett. **108**, 152104 (2016).
[23] A. Ohtomo and Y. Y. Hwang, Nature **427**, 423 (2004).
[24] P. R. Willmott, S. A. Pauli, R. Herger, C. M. Schlepütz, D. Martoccia, B. D. Patterson, B. Delley, R. Clarke, D. Kumah, C. Cionca, and Y. Yacoby, Phys. Rev. Lett. **99**, 155502 (2007).
[25] P. Moetakef, T. A. Cain, D. G. Ouellette, J. Y. Zhang, D. O. Klenov, A. Janotti, C. G. Van de Walle, S. Rajan, S. J. Allen, and S. Stemmer, Appl. Phys. Lett. **99**, 232116 (2011).
[26] J. S. Kim, S. S. A. Seo, M. F. Chisholm, R. K. Kremer, H.-U. Habermeier, B. Keimer, and H. N. Lee, Phys. Rev. B **82**, 201407(R) (2010).
[27] P. Xu, Y. Ayino, C. Cheng, V. S. Pribiag, R. B. Comes, P. V. Sushko, S. A. Chambers, and B. Jalan, Phys. Rev. Lett. **117**, 106803 (2016).
[28] R. Comes, S. R. Spurgeon, S. M. Heald, D. M. Kepaptsoglou, L. Jones, P. V. Ong, M. E. Bowden, Q. M. Ramasse, P. V. Sushko, and S. A. Chambers, Adv. Mater. Interfaces **3**, 1500779 (2016).
[29] H. M. Park, H. J. Lee, S. H. Park, and H. I. Yoo, Acta Crystallogr., Sect. C: Cryst. Struct. Commun. **59**, i117–i119 (2003).
[30] A. M. Glazer, Acta Crystallogr., Sect. B: Struct. Crystallogr. Cryst. Chem. **28**, 3384 (1972).

[31] I. K. Robinson and D. J. Tweet, Rep. Prog. Phys. **55**, 599–651 (1992).
[32] M. Björck and G. Andersson, J. Appl. Cryst. **40**, 1174–1178 (2007).
[33] S. J. May, J.-W. Kim, J. M. Rondinelli, E. Karapetrova, N. A. Spaldin, A. Bhattacharya, and P. J. Ryan, Phys. Rev. B **82**, 014110 (2010).
[34] M. Brahlek, A. K. Choquette, C. R. Smith, R. Engel-Herbert, and S. J. May, J. Appl. Phys. **121**, 045303 (2017).
[35] A. Vailionis, H. Boschker, W. Siemons, E. P. Houwman, D. H. A. Blank, G. Rijnders, and G. Koster, Phys. Rev. B **83**, 064101 (2011).